nature communications

Article

https://doi.org/10.1038/s41467-025-66604-z

Data-driven dynamic modeling for inverter-based resources using neural networks

Received: 23 April 2025

Accepted: 11 November 2025

Published online: 28 November 2025

Check for updates

Ke Yang, Xin Wang, Xunjun Chen, Renshun Wang, Guangchao Geng & Quanyuan Jiang

Dynamic models are a cornerstone of power system stability and control. The growing penetration of inverter-based resources, driven by global decarbonization, significantly complicates power system dynamics. For large-scale power systems, existing dynamic models of these resources have long struggled to accurately capture their complex behaviors, limited primarily by explicit formulations based on simplified physical governing equations. This study presents a data-driven modeling approach that uses neural networks to learn and represent these dynamics exclusively from accessible data. Its tailored architecture combining long short-term memory network for temporal dependencies with a cross layer to model nonlinear feature interactions. Physical constraints from an inverter dynamic model are enforced to enhance consistency and prevent implausible outputs. Validated on a real-world power system (including a wind farm, a photovoltaic power station, and a grid-forming battery energy storage station), the proposed model shows superior accuracy and extrapolates across out-of-distribution scenarios. These findings are further confirmed in a large-scale power system and an inverter-dominated system. The presented approach provides an effective methodology to capture and simulate complex inverter dynamics, enabling more reliable transient stability assessment crucial for the secure operation of future grids.

The transition towards decarbonizing electricity is accelerating globally, driven by substantial increases in renewable energy capacity[1]. Renewable energy is expected to meet all additional electricity demand through 2026[2], with wind and solar power generation already contributing over 40% or even 60% in some countries[3]. Wind and solar power generation require inverter-based interfaces to connect power resources to power grids. Renewable energy sources integrated into the power grid via these interfaces are classified as inverter-based resources (IBRs). The fast and complex dynamic behavior of IBRs, characterized by reduced system inertia, rapid power-electronic transients, and diverse control interactions, complicates the modeling and transient analysis of power systems[4,5]. Given that dynamic models are the cornerstone of power system stability and control[6], several analyses of recent power system disturbances have raised serious concerns about the accuracy of IBR dynamic modeling[7–9], highlighting the need for improved modeling methods to support power system security and stability at higher levels of renewable energy penetration.

The transient analysis of large-scale power systems incorporating IBRs typically relies on time-domain simulations utilizing dynamic models, also known as the root mean square (RMS) model, phasor-domain model, electromechanical transient model, positive sequence model, etc. Despite vendors developing proprietary dynamic models (vendor models), significant concerns have emerged regarding confidentiality and software-specific implementations[10]. Therefore, in 2010, the first-generation generic dynamic models for wind turbines and photovoltaic (PV) systems were released by the Western Electricity Coordinating Council (WECC)[11]. Due to the inherent limitations, such as low accuracy and limited model customization capabilities, the International Electrotechnical Commission (IEC) and WECC

College of Electrical Engineering, Zhejiang University, Hangzhou, China. e-mail: ggc@zju.edu.cn

collaborated to release the second-generation generic models in 2015[12]. These generic models are fundamentally developed using physics-based approaches derived from simplified physical governing equations. Although continuous refinements have been made in the subsequent years[13,14], inherent challenges persist. These limitations stem from several factors: (1) The precise operational mechanisms of IBRs are often obscured by proprietary concerns. Inverter characteristics are primarily dictated by control algorithms, which vendors may not fully disclose for reasons of commercial confidentiality[5,10]. (2) The growing diversity of control strategies employed in inverters, broadly categorized into grid-following and grid-forming paradigms, challenges the efficacy and universality of single generic models. (3) The mismatch in temporal resolution makes it infeasible to explicitly formulate the detailed physical mechanisms, thereby inherently limiting the fidelity and accuracy of the models[5,15]. This is because IBR dynamic models are typically simulated at the millisecond time scale, which is coarser than the microsecond time scale governing the physical processes within some IBR devices of IBRs.

Given these limitations of physics-based approaches, data-driven modeling methods have emerged as a promising alternative. The proliferation of measurement devices, such as wide-area measurement systems (WAMS)[16] and supervisory control and data acquisition (SCADA)[17], facilitates the development of data-driven dynamic models. By using measured data, models can be optimized or tuned to represent the dynamics of IBRs without relying on detailed physical understanding and information. Recent studies[18–20] use measured data to cluster IBRs, and then perform parameter identification to establish dynamic models. These methods, however, may not fully overcome the inherent limitations derived from physics-based modeling methods. Neural networks, with their data-driven nature and powerful expressive capabilities, hold significant potential for addressing the challenges associated with IBR dynamic modeling. Xiao et al.[21] form a neural network-based modeling framework to accurately capture the dynamics of power system components. They further propose a design for power system time-domain simulators to accommodate neural networks[22]. Some studies also analyze and improve the methods for incorporating neural networks into time-domain simulation[23,24]. In ref. 25, a data-driven dynamic model of synchronous generators is proposed. Ref. 26 utilizes the data-driven method to precisely model the profiles and dynamics of the load with IBRs. In ref. 27, a black-box dynamic model for microgrids with IBRs is proposed by using long short-term memory (LSTM). In ref. 25,27, the similarity between LSTM and differential algebraic equations (DAEs) describing power system dynamics is discussed in detail. In ref. 28, a dynamic equivalent model is developed for the hybrid renewable energy source in the form of a deep LSTM network. Ref. 29 proposes a high-precision dynamic modeling framework for PV power stations using LSTM. Despite their ability to achieve high accuracy in dynamic modeling, purely neural network-based approaches inherently lack the capacity to enforce physical laws or integrate prior knowledge, occasionally, leading to physically inconsistent or even implausible predictions[30]. This potential for unreliable outputs poses a significant concern, particularly in safety-critical applications like power system operation and planning[31].

Consequently, a physics-informed neural network (PINN) is proposed by combining physical mechanisms with neural network models[32–34]. This approach has gained significant attention across various power system applications, as summarized in recent reviews[31], and has been adapted for tasks such as creating dynamic equivalents[35] and improving state estimation[36]. However, a primary challenge for applying PINN to IBRs is its reliance on accurate, explicit governing equations. As established previously, such equations are often unavailable due to vendor confidentiality, mismatch in temporal resolution, etc. Furthermore, the multilayer perceptron (MLP), the foundation of PINN, is not suitable for such time-series regression tasks.

In summary, the existing modeling landscape presents a clear challenge: physics-based models struggle with accuracy due to simplifications and proprietary details; purely data-driven models, while accurate, lack physical grounding and can produce implausible results; and PINN is hampered by its reliance on known governing equations.

In this work, we propose a data-driven IBR dynamic model for time-domain simulation, composed of an LSTM, a Cross layer, and a physical Inverter dynamic model (LSTMCI). The Cross layer is designed to capture the interactions, which are important and prevalent in power system dynamics[15,37–40]. LSTMCI uses the advantages of neural networks while ensuring that the dynamic behavior of its output is governed by a physical inverter dynamic model. This design enforces LSTMCI to be strictly constrained by physical mechanisms, providing reliable and accurate outputs. This work aims to enhance foundational transient stability studies by providing such a precise model, thereby supporting more accurate grid planning and operational security assessments.

Results

Design of LSTMCI

The structure of the LSTMCI is shown in Fig. 1. Inspired by the similarity between LSTM and the DAEs that describe IBR dynamics, we employ LSTM as the most fundamental component of the LSTMCI to provide the primary dynamic characteristics of the neural network. To enhance expressive ability, a Cross layer is added to introduce additional interactions. The Cross layer connects to an inverter dynamic model via a fully connected layer (FC), which compresses the variable dimensions to match the inputs required by the inverter model. In this study, the inverter model used is REGC_A[41], a widely adopted generic inverter model of WECC, though other inverter models can also be applied. The outputs of the LSTMCI, I_p and I_q, are generated through the inverter dynamic model, whose inputs are the active and reactive current commands (I_{pcmd} and I_{qcmd}). Neural networks, including LSTM, the Cross layer, and FC, are employed to emulate components other than the inverter, such as energy conversion systems (e.g., wind turbines, PV panels, and battery systems) and various controllers. These networks process input signals, such as voltage and environmental information, to generate corresponding command signals. This structure aligns with the functional design of IBRs. Detailed formulations and algorithm descriptions are provided in “Architecture of the LSTMCI” section, while a comprehensive overview of the data generation process for model training can be found in Supplementary Note 3. The model’s compatibility and adaptability with measured data were further verified, with full details provided in Supplementary Note 11.

Test system and scenarios

To comprehensively analyze the dynamic responses of IBRs, we examine a representative real-world power system located in southeastern China as depicted in Fig. 2. This power system includes 59 buses, 70 transmission lines, 6 synchronous generators, and 3 IBRs, including a wind farm, a PV power station, and a battery energy storage station (BESS). In particular, the BESS is grid-forming, and the remaining are grid-following. While all leverage IBR technology, wind farms, PV power stations, and BESSs exhibit substantial variations in composition, topology, and control. Also, the grid-forming and grid-following IBRs differ significantly in structure, control, and dynamics: grid-following inverters in the wind farm and PV power station rely on phase-locked loops (PLLs) for synchronization, while the grid-forming BESS typically lacks PLLs and instead maintains system frequency and voltage through direct control. Therefore, this paper studies and analyzes the three IBRs as examples. Although they cannot fully

https://doi.org/10.1038/s41467-025-66604-z

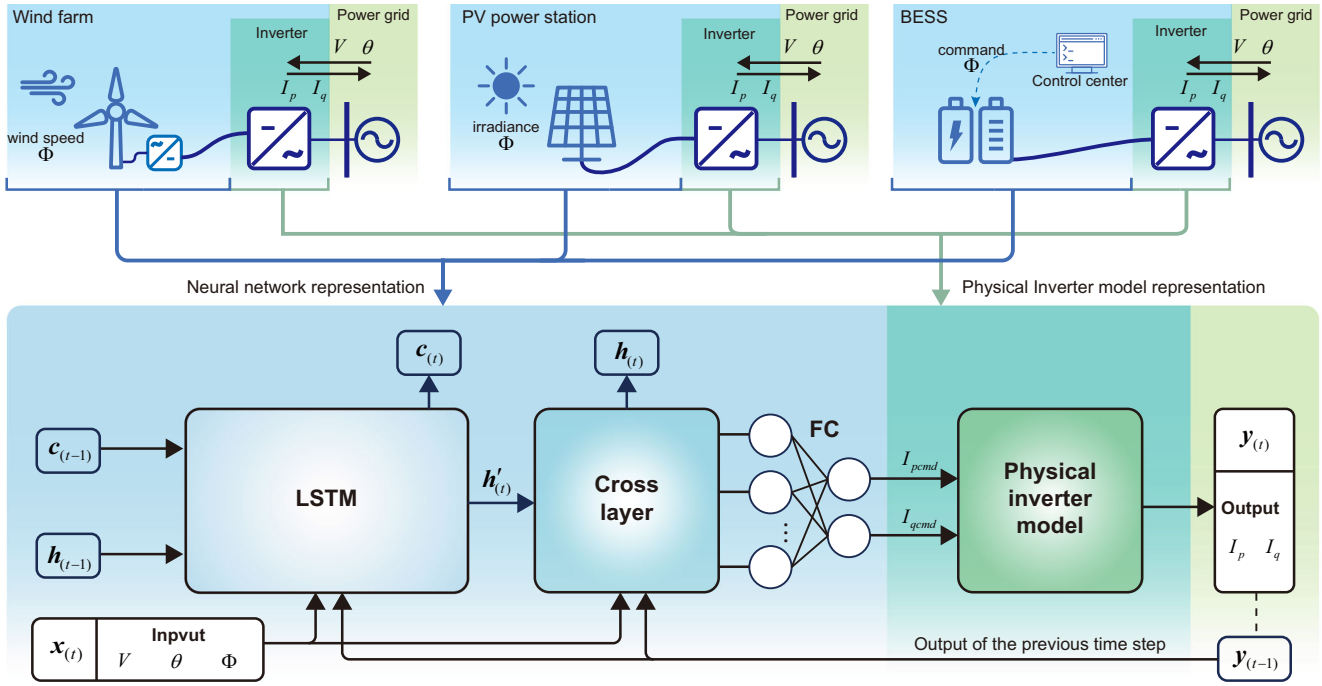

Fig. 1 | The proposed model structure. In this schematic, the top panel shows the structure applied to different inverter-based resources (IBRs), including a wind farm, a photovoltaic (PV) power station, and a battery energy storage station (BESS). In this schematic, t is the time step, $\boldsymbol{h}$ and $\boldsymbol{c}$ are the hidden and cell states, $\boldsymbol{x}$ and $\boldsymbol{y}$ are the input and output variable vectors, respectively. V and θ denote the voltage magnitude and phase angle. The active and reactive currents are given by $I_p = P/V$ and $I_q = Q/V$, where P and Q are the active and reactive power. Φ denotes the other factors, such as environmental information (wind speed, solar irradiance, etc.) and power commands from the control center. Neural networks (including long short-term memory (LSTM), cross-layer, and fully connected layer (FC)) are designed to represent the dynamics beyond inverters. The inverter model simulates the behavior of the inverter and determines the outputs (I_p and I_q) that represent the IBR's interface with the grid.

encompass all of the characteristics of IBRs, they are the most important and widely representative.

The test system is simultaneously constructed in two time-domain simulators: PSD-BPA and an in-house simulator. PSD-BPA is a commercial off-the-shelf (COTS) time-domain simulator[42], where the three IBRs are modeled using their default models, which are based on the second-generation generic model. The parameters of the default model employed in this study are used in practice. The in-house simulator is designed for time-domain simulations utilizing the proposed LSTMCI. Except for the dynamics of the IBRs, the simulation results of the two simulators are consistent (illustrated in Supplementary Note 2).

To validate the differences between the default model of PSD-BPA and the LSTMCI, we subjected three representative examples, one for each of the three IBRs, to four typical disturbances. These disturbances included two low-voltage ride-through (LVRT) scenarios and two high-voltage ride-through (HVRT) scenarios, corresponding to scenarios a, b, c, and d illustrated in Figs. 3–5. All models maintain consistent parameters across the four scenarios. The parameters of the default models are well-suited for scenarios a and c, resulting in the lowest errors in these scenarios compared to the other two. The scenarios and methods of model validation in the examples all satisfy the relevant IEC standard[43]. In addition to these fault-ride-through tests, the model's performance was further validated under a large power mismatch scenario, as detailed in Supplementary Note 7.

To further assess the scalability and practical relevance, we extended our validation to a significantly larger 5,075-bus test system, which is based on an actual regional power grid in China. This large-scale grid contains 496 generators and 10,718 transmission lines, and embeds the 59-bus system described above as a subsystem. Further research and analysis are presented in Supplementary Note 5.

Model validation

Example 1: wind farm. In this example, the target 400 MW wind farm consists of 112 variable-speed wind turbines with permanent magnet synchronous generators (PMSG), each rated at 3.57 MW. Each PMSG is integrated into the medium-voltage collection network through a 0.69 kV/37 kV step-up transformer. The electrical power output is then transmitted via a 35 km medium-voltage collection circuit to a 37 kV/220 kV main transformer, which serves as the point of interconnection to the power grid. The key parameters of a PMSG are listed in S3.

To verify the performance of LSTMCI, we compare two models to the measurements: (1) the default model of the COTS simulator (PSD-BPA) and (2) LSTMCI. The parameters of the default model are actual values used in practice. The outputs of LSTMCI are obtained from the in-house simulator. For a detailed exposition of the model training and integration process with the time-domain simulator, please refer to the "Implementation details" section. The measurements are sampled at the point-of-common coupling (PCC) of the wind farm with a sampling frequency of 100 Hz and processed by a low-pass filter with a cut-off frequency of 1 Hz.

Figure 3 illustrates the simulation results of the proposed model and the default model. To enhance the observability for analytical purposes, the model outputs I_p and I_q have been transformed into P and Q. The default model performs poorly in scenarios b and d, particularly in the voltage recovery curve in scenario b. This is because a single set of default model parameters cannot adequately accommodate all scenarios. Instead, the trained LSTMCI demonstrates enhanced accuracy and adaptability across all scenarios. As depicted in Fig. 3a, b, the proposed LSTMCI model effectively captures key dynamic characteristics, exemplified by the post-fault recovery of active and reactive power.

Figure 3e shows the mean absolute error (MAE) of the four scenarios. The accuracy advantage of the LSTMCI is particularly evident,

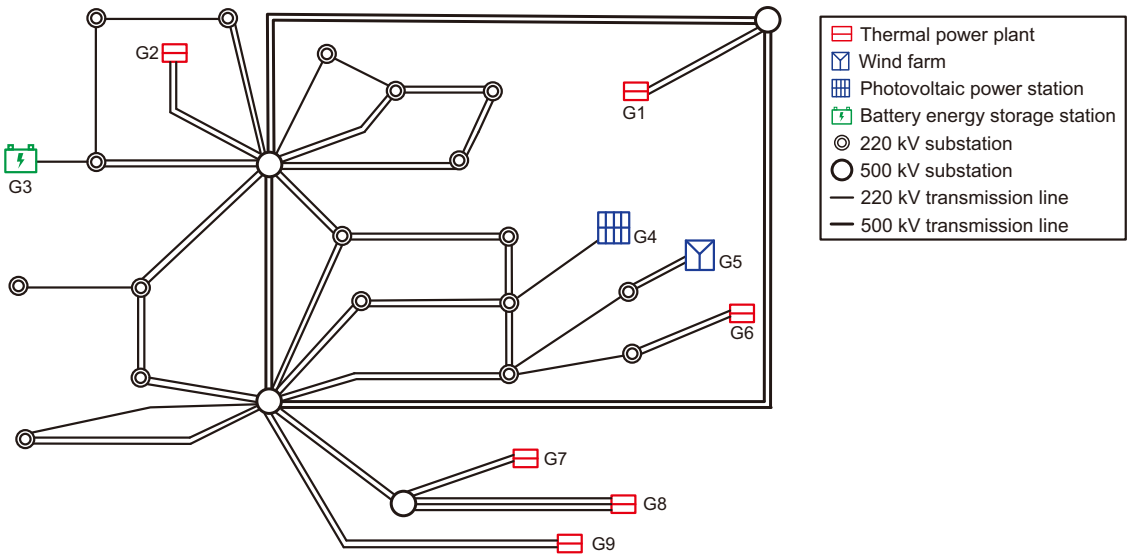

Fig. 2 | Schematic of the test system. The key defines generator types (G1–G9) and substation voltage levels (500 kV and 220 kV). Single, double, and triple lines indicate the number of parallel circuits (one, two, or three) on a transmission corridor. Low-voltage level substations are aggregated for concise illustration.

achieving the lowest error level across almost all scenarios. The mean squared error (MSE) is more sensitive to outliers, providing a perspective that prioritizes the impact of these outliers. Figure 3f shows the MSE of the four scenarios. Across the four scenarios, LSTMCI outperformed the default model, decreasing the overall MAE by 56.1% (from 5.97% to 2.63%) and the MSE by a remarkable 90.9% (from 2.72% to 0.248%). The obvious reduction in MSE suggests that LSTMCI is effective at suppressing large prediction errors and mitigating the extremity of outliers. For more details on error analysis, please refer to Supplementary Note 10. We validated the model's practical workflow through an incremental learning study, which enhanced accuracy in scenario d by fine-tuning with a limited set of measurements (see Supplementary Note 11). It should be noted that while data are normalized for the neural network training process, model outputs are denormalized back to their original physical scale before the calculation of any performance metrics. Therefore, all reported MAE and MSE values are based on the actual per unit (p.u.) values. The definitions of the MAE and the MSE are given by the following:

$$\mathcal{L}_{\mathrm{MAE}} = \frac{1}{N}\sum_{i=1}^{N}|\xi_i - \hat{\xi}_i| \tag{1}$$

$$\mathcal{L}_{\mathrm{MSE}} = \frac{1}{N}\sum_{i=1}^{N}\left(\xi_i - \hat{\xi}_i\right)^2 \tag{2}$$

where $\mathcal{L}_{\mathrm{MAE}}$ and $\mathcal{L}_{\mathrm{MSE}}$ represent the MAE and MSE, respectively. ξ_i is true value at time step i, $\hat{\xi}_i$ is model output at time step i, and N is the number of all data points.

Example 2: PV power station. In this example, the PV power station (rated at 500 MW) comprises 500 PV panels, each rated at 1.05 MW. The brief parameters of a PV panel are listed in S4. Each PV string is connected to the collection system via a 1.14 kV/37 kV step-up transformer. Here, we also compare the performance of the default model and the proposed LSTMCI with the measurements. Measurements are also sampled at the PCC of the PV power station with a sampling frequency of 100 Hz and processed by a low-pass filter with a cutoff frequency of 1 Hz. Figure 4 presents a comparative analysis of four different scenarios.

In scenarios a and b shown in Fig. 4a, b, the default model suffers from overshooting during the power recovery phase after the LVRT. In scenarios c, d, the default model exhibits deviations during the occurrence and recovery of the HVRT process. Figure 4e, f show the MAE and MSE of the default model and LSTMCI relative to the measurement. The default model exhibits poorer MAE and MSE in scenarios b, d. This further highlights the default model's inability to perform accurately in all scenarios, underscoring the limitations of the existing dynamic model of IBRs in terms of accuracy. Across four scenarios, LSTMCI reduced errors compared to the default model, lowering the overall MAE by 70.4% (from 4.53% to 1.34%) and the MSE by 91.1% (from 1.95% to 0.174%). The LSTMCI demonstrates a significant accuracy advantage across all scenarios, aligning more closely with the measured data.

Example 3: grid-forming BESS. The previously analyzed wind farm and PV power station operate with grid-following inverters, which depend on the grid to provide voltage and command signals for maintaining power output. During outages, these inverters disconnect rather than actively contribute to system recovery. In contrast, grid-forming inverters have garnered significant attention for their ability to enhance system stability by autonomously regulating voltage and frequency. To further investigate this capability, we validate a 100 MW/200 MWh grid-forming BESS. The BESS is at the planning stage. The measurements are from field tests and processed by a low-pass filter with a cut-off frequency of 1 Hz.

Figure 5 shows the comparison results between the LSTMCI and the default model of the PSD-BPA. As in the above examples, the parameters of the default model here are optimized and suited for scenarios a and c. The specific parameters tuned for each of the default models are detailed in Supplementary Note 6. Compared to the modeling results for the grid-following wind farm and PV power station (presented in Figs. 3 and 4), the default model exhibits insufficient accuracy in capturing reactive power dynamics during disturbance processes and performs poorly in unoptimized scenarios. These limitations are absent in the LSTMCI model. As shown in Fig. 5e, f, LSTMCI achieves significantly lower MAE and MSE across all four scenarios. Across the four scenarios, LSTMCI significantly outperformed the default model, decreasing the overall MAE by 73.8% (from 8.04% to 2.11%) and the MSE by 94.9% (from 2.83% to 0.145%). This highlights LSTMCI's capability to accurately model grid-forming inverter and BESS dynamics.

https://doi.org/10.1038/s41467-025-66604-z

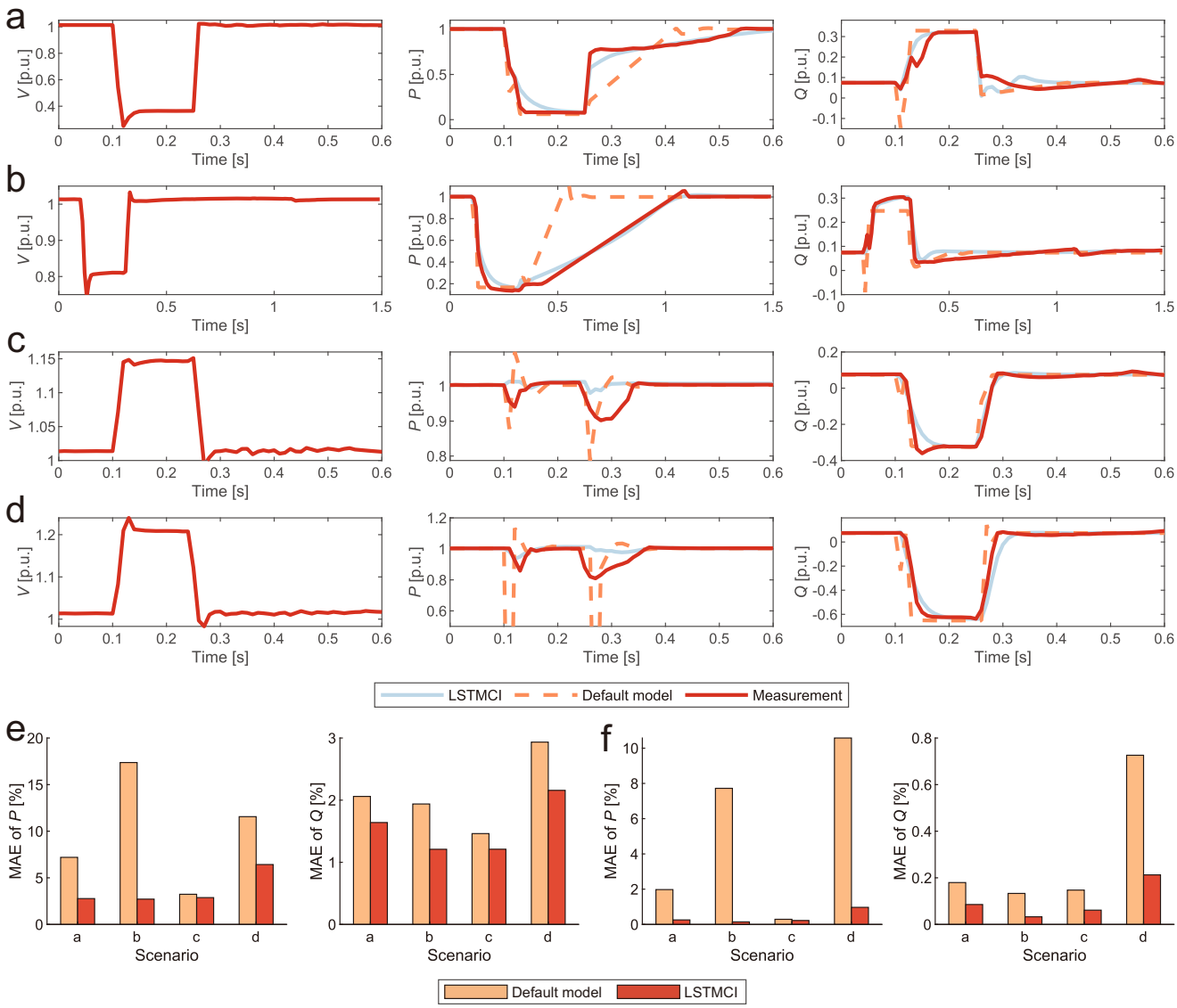

Fig. 3 | Validation of the modeling wind farm. a A low-voltage ride-through (LVRT) scenario (the voltage drops to 0.39 per unit (p.u.)). **b** A LVRT scenario (the voltage drops to 0.83 p.u.). **c** A high-voltage ride-through (HVRT) scenario (the voltage rises to 1.15 p.u.). **d** A HVRT scenario (the voltage rises to 1.22 p.u.). The curves of V show the voltage dips for each scenario. **e** The mean absolute error (MAE) analysis of P and Q between the four scenarios. **f** The mean square error (MSE) analysis. Source data are provided as a Source Data file.

Time-domain simulation with LSTMCI

The superior accuracy of LSTMCI demonstrated across the three examples exhibits notable deviations compared to existing generic dynamic models of IBRs in specific scenarios, thereby allowing for more accurate power system stability assessments.

To investigate these implications, a severe three-phase ground fault is applied at the largest generator of the test system, G1. This event triggers low-frequency oscillations in the rotor angle of the grid, as illustrated in Fig. 6 for simulations employing the vendor model, LSTMCI, and a default model (with consistent parameters maintained across all simulations for a fair comparison). Vendor models, widely regarded within the industry as the most accurate and detailed representations, nevertheless suffer from significant practical drawbacks: they are computationally intensive, proprietary, and tied to specific software platforms[10,44]. These limitations render them unsuitable for the large-scale dynamic studies required by the industry and consequently motivate efforts, such as those by WECC and IEC, to develop generic dynamic models[13]. Notably, Fig. 6 shows that the rotor angle response simulated with LSTMCI closely mirrors the vendor model's results, while the response using the default model exhibits a distinctly different oscillatory pattern. The stability characteristics of these oscillations are quantified below using Prony analysis.

To further characterize these oscillations, Prony analysis is conducted on the rotor angle responses to extract dominant modes[45,46]. The Prony analysis results of rotor angle low-frequency oscillations in generator G2 are summarized in Table 1, where the frequency, amplitude, phase, damping, and damping ratio are provided for each model. The simulations based on the vendor model and LSTMCI both reveal a dominant low-frequency mode, with closely aligned frequencies (0.799 Hz and 0.794 Hz, respectively). Critically, both the vendor model and LSTMCI simulations yield positive damping values (0.020 and 0.021) and corresponding negative damping ratios (−0.395 and −0.411), indicating an unstable response under the fault scenario. In contrast, the simulation using the default model exhibits a different oscillatory profile, characterized by a slightly higher frequency (0.887 Hz), a negative damping value (−0.005), and a corresponding positive damping ratio (0.024), suggesting a stable mode.

https://doi.org/10.1038/s41467-025-66604-z

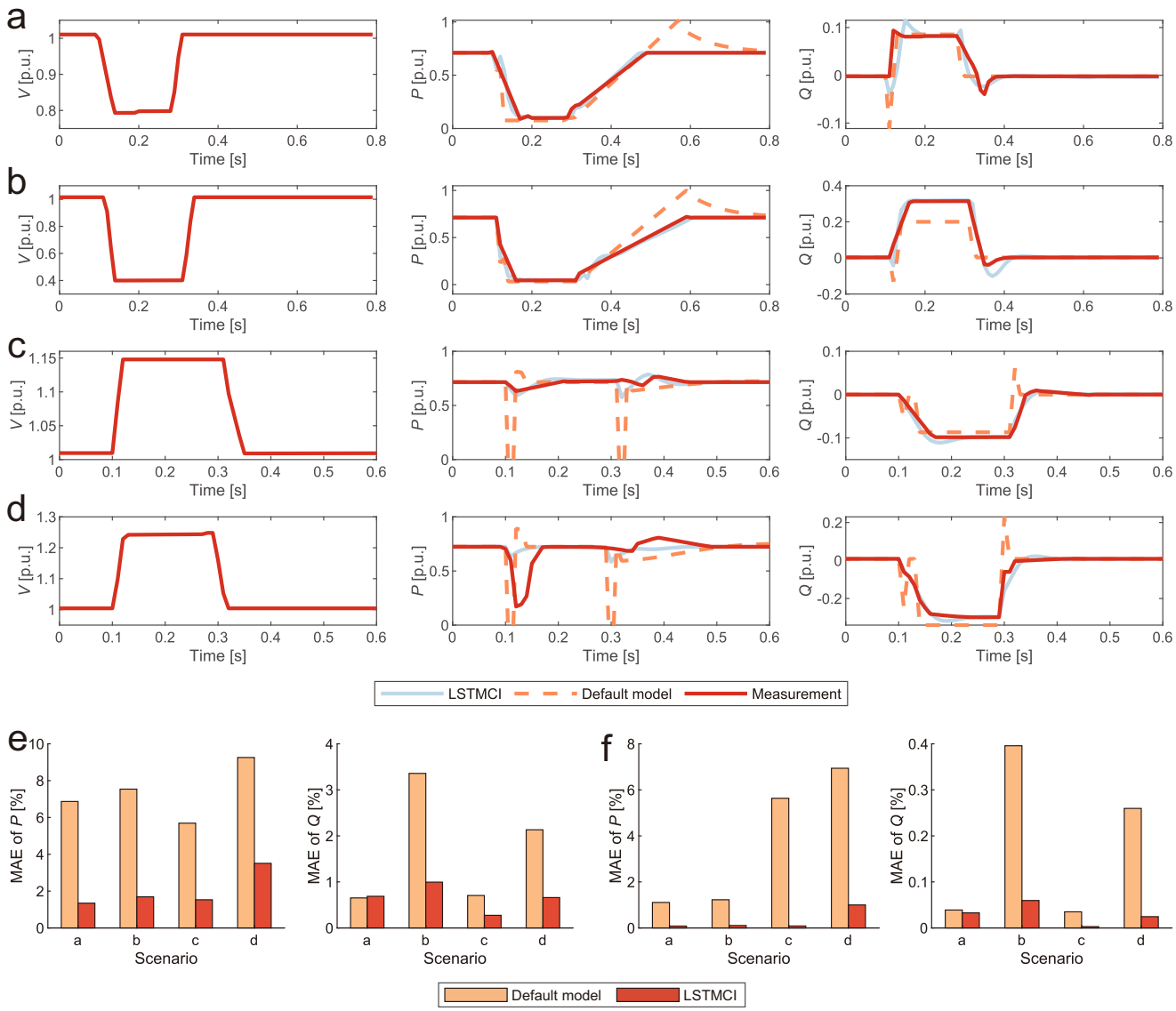

Fig. 4 | Validation of modeling photovoltaic power station. The validation scenarios (**a**–**d**) are defined in Fig. 3. **e** The mean absolute error (MAE) analysis of *P* and *Q* between the four scenarios. **f** The mean square error (MSE) analysis. Source data are provided as a Source Data file.

These Prony analysis findings highlight the significant accuracy improvements of time-domain simulations with LSTMCI. By accurately capturing the dominant oscillatory behavior and the instability tendency predicted by the baseline vendor model, LSTMCI offers a more reliable assessment of power system stability compared to the default model, which exhibits qualitatively different and potentially erroneous stability characteristics. This highlights the importance of employing accurate IBR dynamic models, such as LSTMCI, for comprehensive power system stability studies in power systems with high IBR penetration. To further underscore this point, a detailed comparative analysis in an IBR-dominated, low-inertia system, where the impact of model accuracy is even more critical, is provided in Supplementary Note 9.

Performance comparison

This section validates the proposed LSTMCI model by comparing its extrapolation capability against the default model, and its accuracy and efficiency against other data-driven approaches (including purely neural networks and a PINN). These comparisons serve to demonstrate the superiority of our tailored architecture.

Extrapolation capability. Model evaluation distinguishes between in-distribution data, resembling the training data, and out-of-distribution data, representing novel conditions or out-of-range inputs. Model generalization capability hinges on its extrapolation capability: accurate predictions on out-of-distribution inputs, demonstrating generalization beyond training patterns[47,48]. To validate the extrapolation capability of the model across different scenarios, we tested a continuous LVRT scenario for a wind farm. Initially, the wind farm drops down to 0.4 p.u. 200 ms later, a zone-based protection operates, then the PCC voltage of the wind farm returns to 0.75 p.u. Another protection operates 400 ms later, which returns the voltage to normal. In this scenario, we evaluated the performance of the vendor model, the default model, and the LSTMCI. The time-domain simulation results for each model are shown in Fig. 7a. It is important to note that the training data for LSTMCI is based on single disturbances only. Thus, the blue region in Fig. 7a is within the distribution of the training set or in-distribution, and the other region is out-of-distribution. Despite operating in an untrained scenario, LSTMCI still demonstrated high accuracy. Its dynamic response of the active and reactive power is similar to the vendor model: the MAE between the LSTMCI and the

https://doi.org/10.1038/s41467-025-66604-z

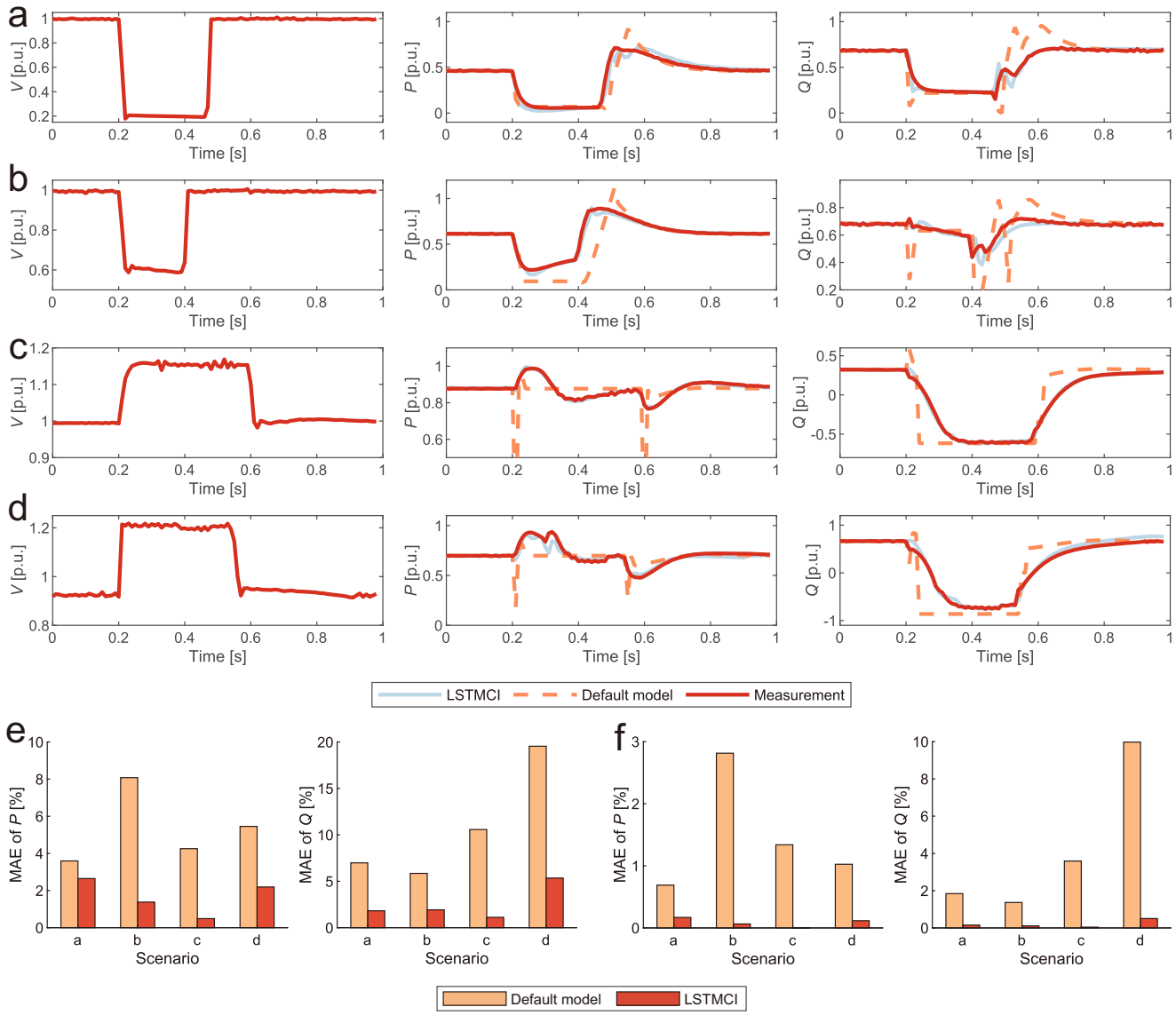

Fig. 5 | Validation of the modeling of the battery energy storage station. The validation scenarios (**a**–**d**) are defined in Fig. 3. **e** The mean absolute error (MAE) analysis of *P* and *Q* between the four scenarios. **f** The mean square error (MSE) analysis. Source data are provided as a Source Data file.

vendor model is 2.04% for active power and 0.73% for reactive power. The default model here is specifically tuned for the 0.4 p.u. LVRT scenario, but it performed poorly in this complex scenario, especially in capturing the active power recovery characteristics. The MAE between the default model and vendor models is 13.61% for active power and 2.62% for reactive power. This illustrates that the default model cannot achieve high accuracy across all scenarios. It highlights that the extrapolation capability of LSTMCI is better across multiple scenarios.

Comparison with other neural networks. Compared to other existing neural network models, our method has distinct theoretical advantages: the outputs of our method are more reliable and explainable. The output of our method is generated by an inverter model, and its dynamic behaviors are compelled to meet the physical constraints of the inverter.

Basically, the IBR dynamic modeling is a time-series regression problem. To provide comparative benchmarks, we evaluated several established sequence models against our proposed approach, including LSTM, RNN, gated recurrent unit (GRU), temporal convolutional neural network (TCN)[49], and Transformer[50]. Furthermore, to situate our work in the context of physics-informed methods, we also include a state-of-the-art PINN in our comparison[51]. The PINN is constructed using the second-generation generic model equations as its physical basis. In order to ensure a fair comparison, the data used for the training of each model, the data normalization method, etc., are kept consistent. Additionally, when feasible, we match the number of parameters of the models to that of the proposed model as closely as possible. Table 2 shows the features of the evaluated models. To reflect the practical scarcity of measured data, the neural network in this study is trained using a limited number of data samples. Details of the data generation process are provided in Supplementary Note 3.

MAEs of the comparison results are shown in Fig. 7b. Among the three examples, the proposed method outperforms all other models, as demonstrated by the fact that the MAEs are at the lowest levels. Among the purely data-driven networks, the MLP shows the maximum errors across the three IBRs, which confirms its unsuitability for time-series regression tasks. The PINN, by incorporating physical information, achieves a lower error than the standard MLP, confirming the benefit of physics-informed approaches. Nevertheless, the proposed LSTMCI model still demonstrates higher accuracy than the PINN across all three IBR cases. This remaining performance gap can be attributed

to the two key limitations of the PINN framework in this application: its accuracy is inherently limited by the accuracy of the simplified generic model equations it relies on, and its MLP-based structure is less adept at capturing complex temporal dependencies compared to LSTMCI. Figure 7d compares the loss function descent process of LSTMCI and LSTM in the validation set. The LSTMCI reaches lower loss faster, which demonstrates better training efficiency.

To determine the optimal structure, this study tested several related alternative structures for the three IBRs validated as examples. Every related alternative structure is detailed in Table 2 and the validation results are shown in Fig. 7c. The error of the LSTM+Inv. is reduced relative to LSTM. This indicates that using the inverter model can effectively regulate the dynamic behavior of LSTM and improve its accuracy. With the Cross layer, the accuracy of LSTM+Cro. is improved relative to LSTM in all scenarios. It shows that the Cross layer adds effective interactions between the variables to LSTM and improves its expressive accuracy. Deep & Cross network (DCN) is specifically designed to provide the interactions[52], but is not effective enough in this problem. DCN provides redundant structures and parameters that complicate the model, resulting in LSTM+DCN+Inv, which is even less accurate than LSTM. The accuracy of RNN+Cro.+Inv. is lower than that of LSTMCI since LSTM is improved from RNN.

Discussion

In this article, we propose a data-driven approach to establishing dynamic models for IBRs, utilizing the advantages of neural networks to overcome the inherent limitations of physics-based, purely neural network-based, and PINN-based dynamic models. The method incorporates physical characteristics by employing an embedded physical inverter model to regulate LSTMCI outputs. This addresses the physical consistency challenges faced by purely neural network-based and PINN-based models. To evaluate its effectiveness, we validated the LSTMCI using two systems: a large-scale, real-world power system containing 5075 buses, and an IBR-dominated system with 57.8% penetration. LSTMCI significantly outperformed existing IBR dynamic models across various scenarios, including complex continuous disturbance events, exhibiting both enhanced extrapolation capability and superior accuracy, with relative reductions of over 90% in MSE and up to 73.8% in MAE. These results highlight the robustness and practical applicability of LSTMCI in power system simulations where diverse conditions and unforeseen fault combinations are common. Consequently, the findings indicate that time-domain simulations incorporating LSTMCI not only enhance simulation accuracy but may also yield transient stability analysis conclusions that differ from those obtained using existing dynamic models of IBRs. Comparing other neural network approaches, LSTMCI achieves higher accuracy with a similar number of parameters due to its physical constraints. This may help alleviate concerns of power system operators about the reliability of neural network-based dynamic models. Furthermore, the proposed LSTMCI approach demonstrates the potential to capture the dynamics of a broad range of IBRs, indicating its applicability extends beyond the specific case studies examined here (e.g., wind farms, PV power stations, and BESSs). Ultimately, by providing a more reliable foundation for time-domain simulation, this methodology has the potential to enhance a range of critical engineering studies, including power system planning, security assessment, post-mortem event analysis, and so on. For further clarification, a schematic illustrating this hierarchical application framework is provided in Supplementary Note 13.

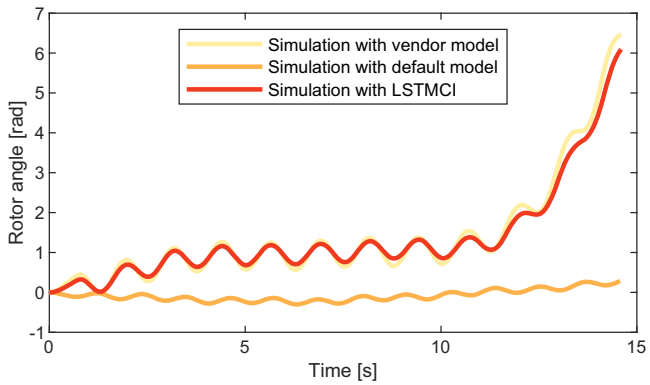

Fig. 6 | Comparison of rotor angle curve observed at the generator G2 relative to G1. For location of the G1 and G2 see Fig. 2. The simulation with the vendor models is shown as a reference, where closer agreement indicates better accuracy. Source data are provided as a Source Data file.

There still remain some potential limitations associated with the present LSTMCI for IBR dynamic modeling. Firstly, the training data of LSTMCI in this study is generated from the vendor models, which are widely recognized by the industry as a benchmark for accuracy. While these models are accurate, they may not fully align with measured data and may not encompass all dynamic behaviors encountered in operational environments. In practice, measured data can be utilized to train the model for further improvement in accuracy. For new installations with scarce data, transfer learning can be employed to adapt a pre-trained model from a similar IBR, significantly accelerating deployment. A further practical consideration is the long-term validity of the model, as IBR characteristics can evolve due to aging or firmware updates, which is a challenge known as concept drift. To counteract concept drift over time, models can be efficiently updated using incremental learning, an approach whose feasibility we have successfully demonstrated in this work (see Supplementary Note 11). To solve the challenge of maintaining long-term accuracy, well-established online adaptation strategies can be employed to automate this process, where performance degradation automatically triggers model fine-tuning. A detailed discussion of these strategies is provided in the Supplementary Note 11. Additionally, when initial training data are insufficient, transfer learning from pre-trained models can enhance accuracy in dynamic modeling. Furthermore, for data-scarce scenarios such as new installations, a practical strategy is to generate training data via detailed electromagnetic transient simulations using vendor models. The use of such simulated data is justified by its superior accuracy over simplified generic models and is a practice supported by recent community efforts in creating open-source datasets for this purpose[53]. This workflow ensures our method's applicability even when extensive historical measurements are unavailable. Practical data quality is also a key consideration. The model's performance is fundamentally linked to the data's temporal resolution; the 100 Hz rate used herein is consistent with WAMS and sufficient for capturing the target dynamics. In terms of measurement accuracy, the model's average Total Vector Error (4.81%) on test data approaches the IEEE standard for measurements (<1% Total Vector Error)[54]. This proximity indicates the model's high accuracy,

Table 1 | Prony analysis results of rotor angle low-frequency oscillations in generator G2

Model used for simulation	Frequency (Hz)	Amplitude (rad)	Phase (rad)	Damping	Damping ratio
Vendor model	0.799	0.288	−1.374	0.020	−0.395
LSTMCI	0.794	0.193	−1.149	0.021	−0.411
Default model	0.887	0.068	1.614	−0.005	0.024

https://doi.org/10.1038/s41467-025-66604-z

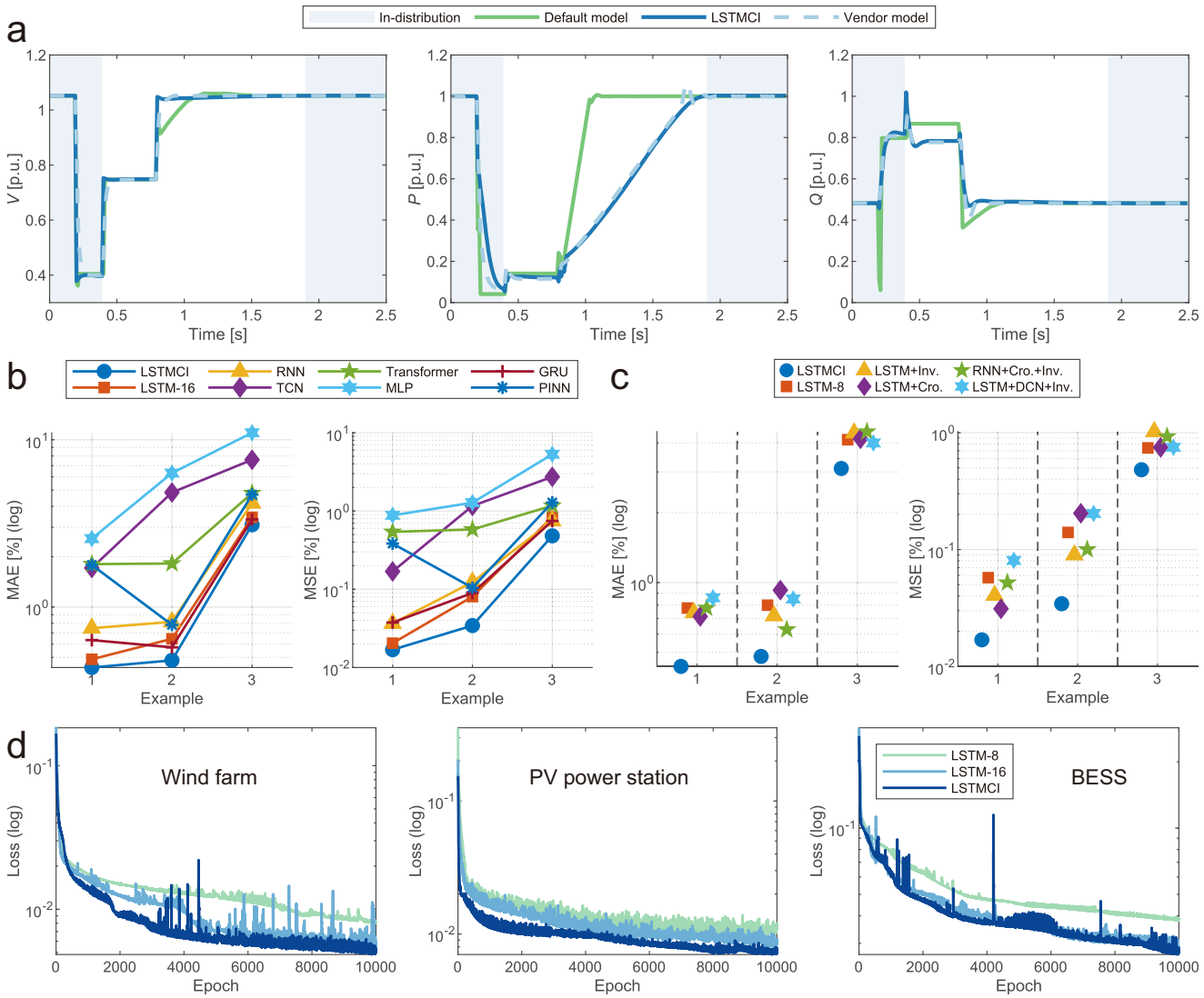

Fig. 7 | Results of performance comparison. a Continuous low-voltage ride-through (LVRT) process observed at the point-of-common coupling (PCC) of the wind farm. The training data of LSTMCI only contains a single disturbance. The blue region represents the trained data, and the other region is untrained. In the beginning, the PCC voltage of the wind farm drops to 0.4 p.u. Then, a zone-based protection is triggered, returning the voltage to 0.75 p.u. A second protection operates 400 ms later, returning the voltage to normal. **b** mean absolute error (MAE) and mean square error (MSE) results of neural networks for the three inverter-based resources (IBRs). The compared models include the recurrent neural network (RNN), temporal convolutional network (TCN), multilayer perceptron (MLP), and gated recurrent unit (GRU). **c** MAE and MSE results of similar structures for the three inverter-based resources (IBRs): the wind farm, photovoltaic (PV) power station, and battery energy storage system (BESS). The inverter dynamic model is denoted as Inv., and the cross-layer is denoted as Cro. **d** Efficiency of training models for the three IBRs. Source data are provided as a Source Data file.

while also suggesting that sensitivity to measurement noise is an important characteristic for future investigation of such high-performance models. Investigating the model's sensitivity to measurement noise, a characteristic challenge for such high-fidelity models, is therefore a key direction for future research. Furthermore, the number of parameters in the Cross layer scales cubically with the number of LSTM hidden layers. Therefore, increasing the number of hidden layers to increase the representational capacity of the model can lead to computational challenges. Based on the results of this study, an LSTMCI model with eight hidden layers is sufficient for the complexity of wind farms, PV power stations, and BESSs. Meanwhile, for IBRs of lower complexity, reducing the number of hidden layers would be beneficial in optimizing the performance and computational efficiency of the model. The independent nature of each LSTMCI instance means that the framework is naturally capable of parallel or distributed computation. This is the recommended approach to ensure computational efficiency, particularly for deployment in large-scale systems with a substantial number of IBRs. A detailed computational benchmark study has confirmed that this approach ensures the framework is both scalable and capable of faster-than-real-time performance (see Supplementary Note 8). Additionally, LSTMCI is sensitive to the initial parameters of the inverter model. This may be attributed to the training algorithm and the structure of the inverter model employed in this study, wherein specific parameters are defined by upper and lower bounds for limiting functions. These parameters are only updated when limits are triggered, leading to low update frequency, which can prevent the optimization of all inverter model parameters to their optimal values. Adjusting the optimization step size for inverter model parameters, optimizing only key parameters, or selecting alternative optimization algorithms for the inverter model could help to address this issue. Accordingly, there exists substantial potential for the enhancement of the performance of LSTMCI.

Moreover, a potential relationship exists between the parameters and computational procedures of the LSTMCI and the fundamental

Table 2 | Model details and descriptions

Model	Number of parameters	Description
LSTM-16	1922	The LSTM with 16 hidden layers.
RNN	1946	The RNN with 24 hidden layers.
GRU	1964	The GRU with 18 hidden layers.
TCN	1946	TCN with 3 convolutional layers (13 channels each).
MLP	1924	MLP with 7 layers (17 neurons each), using Hardtanh as activation function.
PINN	1924	A PINN enforcing the physics of the second-generation generic model as hard constraints, based on the architecture in ref. 51.
Transformer	1939	The Transformer with 5 encoder and decoder layers, 7 multi-head attention heads, an input feature dimension of 7, an 8-dimensional feed-forward network, and a 0.1 dropout rate.
LSTM-8	578	The LSTM with eight hidden layers.
LSTM+Inv.	588	LSTM-8 with an inverter model.
LSTM+Cro.	1207	LSTM-8 with Cross-layer.
RNN+Cro.+Inv.	1628	RNN (8 hidden layers) with cross-layer and inverter model.
LSTM+DCN+Inv.	652	LSTM-8 with DCN and inverter model.
LSTMCI	1940	LSTM-8 with Cross layer and inverter (can also be marked as LSTM+Cro.+Inv.).

The inverter dynamic model is denoted as Inv., and the cross-layer is denoted as Cro. The FCs of the models are set in the same way and are omitted from the description.

physical mechanisms governing IBR dynamics. It is anticipated that techniques such as visualization and sparse regression will facilitate the elucidation of these mechanisms. This investigation will constitute a key component of our future research.

Methods

Architecture of the LSTMCI

The proposed network architecture of LSTMCI is shown in Fig. 1. The model architecture reflects the physical structure of IBRs. LSTMCI uses neural networks, LSTM, Cross layer, and FC to capture and express non-inverter dynamics. Subsequently, an inverter model employs the output of the neural network to generate current for injection into the grid. This study employs an inverter model, REGC_A, and other inverter models are also available. Among the neural networks, the LSTM serves as the foundational element. The selection of LSTM over RNN is due to the fact that RNNs suffer from the vanishing gradient problem, making them ineffective at capturing the crucial long-term dependencies in power system dynamics. Compared to the similarly efficient GRU, the LSTM's more expressive structure with separate forget and input gates allows for more flexible control over the model's memory, which is critical for modeling the complex, path-dependent behavior of IBRs following a disturbance[27–29]. It processes the hidden state of the last time step, $\boldsymbol{h}_{(t-1)}$, cell state of the current time step, $\boldsymbol{c}_{(t-1)}$, and input variable of the current time step $\boldsymbol{x}_{(t)}$, to output the middle hidden state, $\boldsymbol{h}'_{(t)}$. Notably, the input vector $\boldsymbol{x}_{(t)}$ includes voltage magnitude and phase angle, while system frequency is omitted. This is because, within the phasor-domain framework used for transient stability, frequency dynamics are implicitly captured by the time derivative of the phase angle ($\Delta f = \frac{1}{2\pi}\frac{d\theta}{dt}$), making it a learnable but redundant feature. The Cross layer processes $\boldsymbol{h}'_{(t)}$, $\boldsymbol{x}_{(t)}$, and the outputs of the last time step, $\boldsymbol{y}_{(t-1)}$, to output the hidden state, $\boldsymbol{h}_{(t)}$. FC processes $\boldsymbol{h}_{(t)}$ to output the inputs of the REGC_A, I_{pcmd} and I_{qcmd}. In the end, REGC_A outputs I_p and I_q as the output of the LSTMCI. Supplementary Note 1 provides detailed information on the REGC_A model, including its structure, parameters, and practical availability. The LSTMCI offers a unified framework for modeling the dynamics of IBRs. The flexibility of this approach allows for the modeling of diverse IBR types by simply adjusting the inputs to LSTMCI.

A key challenge in IBR dynamic modeling is representing the numerous and significant nonlinear interactions among state variables. Fundamentally, these interactions arise from the underlying physics: for instance, quantities like active and reactive power are products of voltage and current, and the essential d/q-axis transformations central to inverter control involve nonlinear trigonometric functions of the phase angle. While a standard LSTM can capture temporal patterns, it cannot efficiently or explicitly model these crucial pairwise and higher-order feature interactions[25]. To address this, in this study, the cross-layer is designed to add pairwise interactions between all variables (including $\boldsymbol{h}'$, $\boldsymbol{x}$, and $\boldsymbol{y}$) to the LSTM equations. The input of the Cross layer includes $V_{(t)}$, $\theta_{(t)}$, $\Phi_{(t)}$, $I_{p(t-1)}$, and $I_{q(t-1)}$. By multiplying or squaring these variables, relevant electrical power information can be incorporated. The input of the Cross layer also includes $\boldsymbol{h}'$, allowing $\boldsymbol{h}'$ for other inputs of the Cross layer to simulate additional pairwise interactions. The equations of the cross-layer are shown in (3) and (4). The calculation process is depicted in Fig. 8a.

$$\mathcal{I} = (M_h \otimes \boldsymbol{l}^T) W_I \boldsymbol{l} \tag{3}$$

$$\boldsymbol{l} = [\boldsymbol{h}^T_{(t)}, \boldsymbol{x}^T_{(t)}, \boldsymbol{y}^T_{(t-1)}]^T \tag{4}$$

where $\mathcal{I}$ represents all the interactions, W_I denotes weights, $\boldsymbol{l}$ is a column vector composed of all the variables, $\otimes$ is the Kronecker product, M_h is an $n_h \times n_h$ unitary matrix, n_h is the number of dimensions of $\boldsymbol{h}$, also the number of state variables.

Implementation details

Initialization. The parameters of the neural networks of the LSTMCI are initialized with Xavier normal[55], and the parameters of the inverter model are set according to the rated values collected from vendors. The state variables of the LSTM are initialized as zeros, and the variables of the REGC_A are initialized according to the power flow results.

Data preprocessing. The comprehensive overview of the data generation process for model training can be found in Supplementary Note 3. All of the data used is low-pass filtered. For the dynamic model, the signals of the IBRs are centered around the steady-state operating point, with significant deviations occurring during faults. Therefore, we propose a mean centering adjustment based on min-max normalization to normalize the input used by the LSTM and the cross-layer of the LSTMCI. The normalization is defined by the following:

$$\boldsymbol{z}^* = \frac{\boldsymbol{z} - \boldsymbol{z}_{\min}}{\boldsymbol{z}_{\max} - \boldsymbol{z}_{\min}} - \frac{1}{N_i}\sum_{i=1}^{N_i}\frac{\boldsymbol{z} - \boldsymbol{z}_{\min}}{\boldsymbol{z}_{\max} - \boldsymbol{z}_{\min}} \tag{5}$$

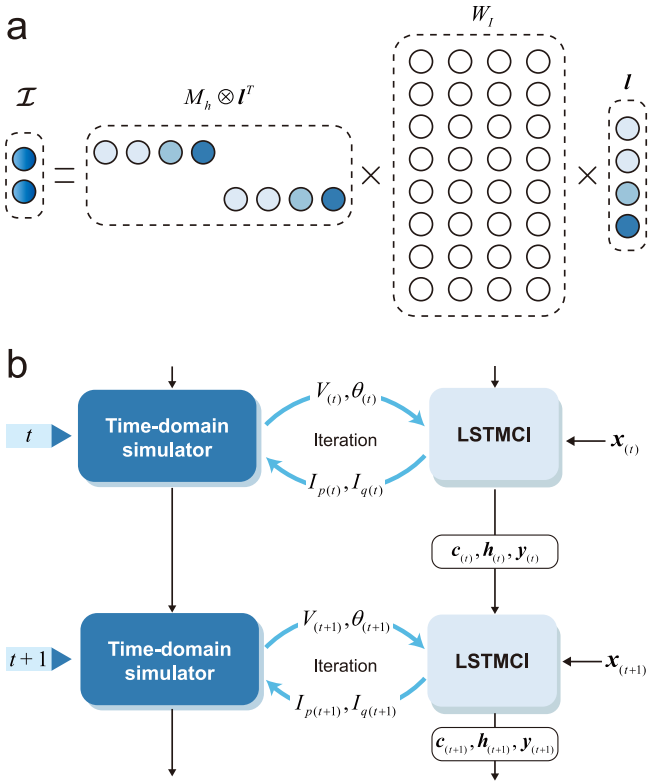

Fig. 8 | Illustration of the cross-layer and the LSTMCI-based time-domain simulation methodology. a Visualization of the proposed cross-layer. **b** Integration process of LSTMCI into a time-domain simulator using the alternating iteration method.

where $\boldsymbol{z}^*$ is the normalized data, $\boldsymbol{z}$ is the original data points, $\boldsymbol{z}_{\min}$ and $\boldsymbol{z}_{\max}$ are the minimum and maximum values of $\boldsymbol{z}$, N_i is the dimension of the $\boldsymbol{z}$.

Training. In this paper, we use the MAE as the evaluation metric, which is commonly used in time-series regression and dynamic model validation[43,56]. The loss function employed by this study is defined as follows:

$$\mathcal{L} = \mathcal{L}_{\mathrm{MAE}}(\boldsymbol{\xi}, \hat{\boldsymbol{\xi}}) + \lambda_k \mathcal{L}_{\mathrm{MAE}}(\boldsymbol{\xi}_k, \hat{\boldsymbol{\xi}}_k) \tag{6}$$

where $\mathcal{L}_{\mathrm{MAE}}$ is the MAE function referring to (1), $\hat{\boldsymbol{\xi}}$ is the output of the LSTMCI, $\hat{\boldsymbol{\xi}}_k$ is the output of the LSTMCI during the key time period (i.e., pre-fault, fault, and post-fault period), $\boldsymbol{\xi}$ and $\boldsymbol{\xi}_k$ are the corresponding true values, and λ_k is a parameter which controls the importance of the key time period.

We select the pre-fault period as the key time period in the loss function to ensure the model accurately establishes the initial steady-state conditions. Furthermore, to develop a more physically grounded internal state representation, the model can be trained to predict key physical quantities in addition to its primary outputs. This is achieved through a multi-task learning strategy. In addition to the primary task of predicting terminal quantities (e.g., currents I_p and I_q), the model is simultaneously trained to predict a set of auxiliary physical variables. These auxiliary targets are selected based on two criteria: their physical significance in representing the IBR's internal dynamics and their practical availability from measurement data (e.g., DC-link voltage, PLL states). This is achieved by defining a composite loss function as shown in Eq. (6), which includes weighted loss terms for both the primary and auxiliary outputs. This process encourages the network to learn a more complete and accurate representation of the IBR's internal dynamics if the internal state's physical quantities can be obtained.

We use the adaptive moment estimation (Adam) optimizer[57] with a batch size of 4 to optimize the parameters of the models. The step size is set to 0.001, the decay rate for momentum is 0.9, and the decay rate for squared gradients is 0.999. All the parameters, including the parameters of the neural networks and the inverter model, are optimized in a synchronous manner. In this study, the neural networks and the REGC_A model are constructed and trained using PyTorch[58].

Representation of different control strategies. The proposed data-driven framework accounts for various IBR control strategies, such as grid-following and grid-forming, by learning their resultant dynamic behaviors. It is important to clarify that while these control strategies correspond to physically different characteristics (i.e., controlled current sources and controlled voltage sources), the model's structure of providing a current injection as output based on terminal voltage as an input is consistent for both. This input-output format is dictated by the standard numerical interface of large-scale time-domain simulators, which requires all component models to provide their corresponding current injections.

Therefore, the model learns to replicate the correct current injection response for any given control strategy within this simulation-compatible modeling framework. Rather than containing explicit parameters or switches for different control modes, the model learns from operational data that inherently embeds the unique dynamic characteristics produced by a specific control strategy in response to grid events. By training on a dataset from an IBR with a grid-forming scheme, for instance, the LSTMCI model learns to replicate that specific grid-forming behavior. Differentiation between control types is thus achieved by training distinct model instances on representative datasets for each strategy. This universal modeling philosophy is illustrated schematically in Supplementary Note 12.

Integration with the time-domain simulator. The proposed model is incorporated into a time-domain simulator using the alternating iteration method, a widely used technique in COTS time-domain simulation software for power systems[23]. Figure 8b shows the brief process of LSTMCI incorporation into a time-domain simulator. At each time step of the alternating iteration, the time-domain simulator feeds the bus voltages to the dynamic models, which in turn feed the injected currents back to the simulator. Once the alternating iteration converges, the solution proceeds to the next time step. At this point, the dynamic model saves and transfers the converged state variables for use in the next time step. Please see Supplementary Note 2 for details.

Data availability

The primary code, models, and datasets generated and analyzed during this study[59] are publicly available in a Code Ocean capsule at https://doi.org/10.24433/CO.7945591.v2. The real-world measurement data and the detailed parameters for the 5075-bus power system are confidential and are not available due to regulations from the grid operator. The source data underlying the figures in this paper are provided in the Source Data file.

Code availability

The codes necessary for reproducing the results of the manuscript are available on Code Ocean at https://doi.org/10.24433/CO.7945591.v2.

References

1. IEA: Renewables 2024. https://www.iea.org/reports/renewables-2024 (2024).

2. IEA: Electricity 2024. https://www.iea.org/reports/electricity-2024/ (2024).
3. EMBER: Global electricity review 2024. https://ember-climate.org/insights/research/global-electricity-review-2024/ (2024).
4. Sajadi, A., Kenyon, R. W. & Hodge, B.-M. Synchronization in electric power networks with inherent heterogeneity up to 100% inverter-based renewable generation. *Nat. Commun.* **13**, 2490 (2022).
5. Gu, Y. & Green, T. C. Power system stability with a high penetration of inverter-based resources. *Proc. IEEE* **111**, 832–853 (2023).
6. Shair, J., Li, H., Hu, J. & Xie, X. Power system stability issues, classifications and research prospects in the context of high-penetration of renewables and power electronics. *Renew. Sustain. Energy Rev.* **145**, 111111 (2021).
7. NESO: technical report on the events of 9 August 2019. https://www.neso.energy/document/152346/download (2019).
8. NERC: Multiple solar PV disturbances in CAISO between June and August 2021. https://www.nerc.com/pa/rrm/ea/Documents/NERC_2021_California_Solar_PV_Disturbances_Report.pdf (2021).
9. Joint NERC and Texas RE Staff Report: Odessa disturbance Texas events: May 9, 2021 and June 26, 2021. https://www.nerc.com/pa/rrm/ea/Documents/Odessa_Disturbance_Report.pdf (2021).
10. NREL: Comparison of standard wind turbine models with vendor models for power system stability analysis. https://www.nrel.gov/docs/fy17osti/67249.pdf (2016).
11. WECC: WECC wind power plant dynamic modeling guide. https://transmission.bpa.gov/Business/Operations/GridModeling/WECCWindPlantDynamicModelingGuide.pdf (2010).
12. IEC 61400-27-1: Wind energy generation systems - Part 27-1: Electrical simulation models - Generic models (2015).
13. IEC 61400-27-1: Wind energy generation systems - Part 27-1: Electrical simulation models - Generic models (2020).
14. Ramasubramanian, D. et al. Positive sequence voltage source converter mathematical model for use in low short circuit systems. *IET Gener. Transm. Dis.* **14**, 87–97 (2020).
15. Witthaut, D. et al. Collective nonlinear dynamics and self-organization in decentralized power grids. *Rev. Mod. Phys.* **94**, 015005 (2022).
16. Vahidi, S. et al. Security of wide-area monitoring, protection, and control (WAMPAC) systems of the smart grid: a survey on challenges and opportunities. *IEEE Commun. Surv. Tutor.* **25**, 1294–1335 (2023).
17. Cheng, G., Lin, Y., Abur, A., Gómez-Expósito, A. & Wu, W. A survey of power system state estimation using multiple data sources: PMUs, SCADA, AMI, and beyond. *IEEE Trans. Smart Grid* **15**, 1129–1151 (2024).
18. Radovanović, A. & Milanović, J. V. Equivalent modelling of hybrid RES plant for power system transient stability studies. *IEEE Trans. Power Syst.* **37**, 847–859 (2022).
19. Zhang, J., Cui, M. & He, Y. Robustness and adaptability analysis for equivalent model of doubly fed induction generator wind farm using measured data. *Appl. Energy* **261**, 114362 (2020).
20. Wang, P. et al. Improved wind farm aggregated modeling method for large-scale power system stability studies. *IEEE Trans. Power Syst.* **33**, 6332–6342 (2018).
21. Xiao, T., Chen, Y., Huang, S., He, T. & Guan, H. Feasibility study of neural ODE and DAE modules for power system dynamic component modeling. *IEEE Trans. Power Syst.* **38**, 2666–2678 (2023).
22. Xiao, T. et al. Exploration of artificial-intelligence oriented power system dynamic simulators. *J. Mod. Power Syst. Clean. Energy* **11**, 401–411 (2023).
23. Wang, X., Yang, K., Geng, G. & Jiang, Q. Convergence enhancement for neural network integrated power system time domain simulation. *IEEE Trans. Power Syst.* **40**, 1481–1491 (2025).
24. Wang, X. et al. A fast electromechanical transient simulation algorithm for power system based on data and physics-driven model. *Proc. CSEE* **44**, 2955–2965 (2024).
25. Yang, K., Wang, X., Ling, J., Geng, G. & Jiang, Q. Modeling of synchronous generator based on physics-informed neural network. *Proc. CSEE* **44**, 4924–4933 (2024).
26. Anvari, M. et al. Data-driven load profiles and the dynamics of residential electricity consumption. *Nat. Commun.* **13**, 4593 (2022).
27. Li, Y. et al. Dynamic equivalent modeling for black-box microgrids under multi-operating-point by using LSTM. *CSEE J. Power Energy Syst.* **10**, 639–648 (2024).
28. Radovanović, A. & Milanović, J. V. Deep learning-based equivalent modelling of hybrid RES plant for efficient, repetitive power system transient stability studies. *IEEE Trans. Power Syst.* **39**, 3008–3020 (2024).
29. Li, P. et al. High-precision dynamic modeling of two-staged photovoltaic power station clusters. *IEEE Trans. Power Syst.* **34**, 4393–4407 (2019).
30. Karniadakis, G. E. et al. Physics-informed machine learning. *Nat. Rev. Phys.* **3**, 422–440 (2021).
31. Huang, B. & Wang, J. Applications of physics-informed neural networks in power systems-a review. *IEEE Trans. Power Syst.* **38**, 572–588 (2023).
32. Raissi, M., Perdikaris, P. & Karniadakis, G. E. Physics-informed neural networks: a deep learning framework for solving forward and inverse problems involving nonlinear partial differential equations. *J. Comput. Phys.* **378**, 686–707 (2019).
33. Chen, Z., Liu, Y. & Sun, H. Physics-informed learning of governing equations from scarce data. *Nat. Commun.* **12**, 6136 (2021).
34. Bian, L. et al. High-resolution single-photon imaging with physics-informed deep learning. *Nat. Commun.* **14**, 5902 (2023).
35. Shen, Q. et al. Physics-aware neural dynamic equivalence of power systems. *IEEE Trans. Power Syst.* **39**, 2341–2344 (2024).
36. Ngo, Q.-H., Nguyen, B. L. H., Vu, T. V., Zhang, J. & Ngo, T. Physics-informed graphical neural network for power system state estimation. *Appl. Energy* **358**, 122602 (2024).
37. Ganmor, E., Segev, R. & Schneidman, E. Sparse low-order interaction network underlies a highly correlated and learnable neural population code. *Proc. Natl Acad. Sci.* **108**, 9679–9684 (2011).
38. Battiston, F. et al. Networks beyond pairwise interactions: structure and dynamics. *Phys. Rep.* **874**, 1–92 (2020).
39. Battiston, F. et al. The physics of higher-order interactions in complex systems. *Nat. Phys.* **17**, 1093–1098 (2021).
40. Li, X. et al. Higher-order granger reservoir computing: Simultaneously achieving scalable complex structures inference and accurate dynamics prediction. *Nat. Commun.* **15**, 2506 (2024).
41. WECC: WECC guide for representation of photovoltaic systems in large-scale load flow simulations (2010).
42. Yin, Y., Tang, Y.: PSD-ST Transient Stabilization Program User Manual Version 5.9. Beijing (CEPRI, 2023).
43. IEC 61400-27-2: Wind energy generation systems - Part 27-2: Electrical simulation models - Model validation (2020).
44. Pourbeik, P. et al. Generic dynamic models for modeling wind power plants and other renewable technologies in large-scale power system studies. *IEEE Trans. Energy Convers.* **32**, 1108–1116 (2017).
45. Khodaparast, J., Fosso, O. B. & Molinas, M. Recursive multi-channel Prony for PMU. *IEEE Trans. Power Del.* **39**, 693–705 (2024).
46. Džafić, I., Jabr, R. A. & Čolo, N. Enhancing Prony's method for fault location. *Int. J. Electr. Power Energy Syst.* **143**, 108476 (2022).
47. Caro, M. C. et al. Out-of-distribution generalization for learning quantum dynamics. *Nat. Commun.* **14**, 3751 (2023).
48. Cui, T. et al. Online test-time adaptation for better generalization of interatomic potentials to out-of-distribution data. *Nat. Commun.* **16**, 1891 (2025).
49. Lea, C., Vidal, R., Reiter, A., Hager, G.D.: Temporal convolutional networks: a unified approach to action segmentation. *arXiv* https://arxiv.org/abs/1608.08242 (2016).

50. Vaswani, A. et al. Attention is all you need. https://arxiv.org/abs/1706.03762 (2023).
51. Lu, L. et al. Physics-informed neural networks with hard constraints for inverse design. *SIAM J. Sci. Comput.* **43**, 1105–1132 (2021).
52. Wang, R. et al. DCN V2: improved deep & cross network and practical lessons for web-scale learning to rank systems. In: *Proc. of the Web Conference 2021*, pp. 1785–1797 (ACM, 2021).
53. Ross, B. & Mahapatra, K. IRTSD: open-source data and toolset for electromagnetic transient analysis of disturbances and IBR control malfunctions in transmission systems. https://doi.org/10.21227/mp6d-j677 (2024).
54. IEEE standard for synchrophasor measurements for power systems. In *IEEE Std C37.118.1–2011* (2011).
55. Glorot, X., Bordes, A. & Bengio, Y. Deep sparse rectifier neural networks. In *Proceedings of the Fourteenth International Conference on Artificial Intelligence and Statistics*, pp. 315–323 (PMLR, 2011).
56. WECC: Solar photovoltaic power plant modeling and validation guideline. https://www.wecc.org/wecc-document/13411 (2019).
57. Kingma, D. P. Adam: a method for stochastic optimization. In *Proceedings of the 3rd International Conference on Learning Representations* (ICLR, 2015).
58. Paszke, A. et al. PyTorch: an imperative style, high-performance deep learning library. *arXiv* https://arxiv.org/abs/1912.01703 (2019).
59. Ke, Y. et al. LSTMCI: a data-driven dynamic model for inverter-based resources. *Code Ocean* https://doi.org/10.24433/CO.7945591.v2 (2025).

Acknowledgements

Q.J. and G.G. were supported by the National Key R&D Program of China (Grant no. 2022YFB2403000). G.G. was supported by the National Natural Science Foundation of China (Grant no. 52177120). The authors thank Guoxiao Gan, Yuhan Jiang, and Rong Yan for their contributions to the analysis and discussion.

Author contributions

The conceptual approach and research design were performed by K.Y. and G.G., with the majority of the analytical and numerical analyses carried out by K.Y., X.W., X.C. and R.W. All authors contributed substantially to the discussion of the content. Q.J. supervised the project. K.Y. wrote the article. All authors contributed to editing the manuscript.

Competing interests

The authors declare no competing interests.

Additional information

Supplementary information The online version contains supplementary material available at https://doi.org/10.1038/s41467-025-66604-z.

Correspondence and requests for materials should be addressed to Guangchao Geng.

Peer review information *Nature Communications* thanks Anil Pahwa, Chia-Chi Chu, Fei Ding and Yu Fujimoto, who co-reviewed with Nanae Kaneko and the other anonymous, reviewer for their contribution to the peer review of this work. A peer review file is available.